AIAA JOURNAL
Vol. 44, No. 6, June 2006

Comparison of Hybrid Turbulence Models for a Circular Cylinder and a Cavity

R. H. Nichols*
University of Alabama at Birmingham, Birmingham, Alabama 35294

Three hybrid Reynolds-averaged Navier–Stokes/large-eddy simulation turbulence models are applied to the flow over a three-dimensional circular cylinder and a generic weapons bay. Time-step and grid sensitivity studies are performed. The time-step study indicates that 100–200 steps per primary shedding cycle are required for temporal accuracy using a second-order implicit algorithm. The grid study indicates that these new turbulence models can achieve a reasonably grid-independent solution in simulation of unsteady turbulent flows. As the mesh resolution is increased, smaller scale turbulent structures become visible. A computational mesh with a grid resolution resulting in a ratio of the turbulent length scale to grid length scale greater than 2 produced a reasonable simulation with all three hybrid models for both cases.

Nomenclature

C_{DES}	=	coefficient for Spalart–Allmaras detached-eddy simulation (DES) hybrid turbulence model
$C_{\mathrm{DES}KE}$, $C_{\mathrm{DES}KW}$	=	coefficients for shear stress transport (SST) DES hybrid turbulence model
C_d	=	drag coefficient
$C_{d\mathrm{corrected}}$	=	corrected drag coefficient
$C_{d\mathrm{measured}}$	=	measured drag coefficient
C_l	=	lift coefficient
d	=	distance from the wall
$\tilde{d}$	=	modified distance defined in Eq. (1)
F_1	=	SST model switching function
f_d	=	SST–multiscale (MS) hybrid model damping function defined in Eq. (8)
k	=	turbulent kinetic energy
k_{LES}	=	subgrid turbulent kinetic energy
k_{RANS}	=	Reynolds-averaged Navier–Stokes (RANS) model turbulent kinetic energy
L_g	=	local grid length scale
L_t	=	local turbulent length scale
Sr	=	Strouhal number
β^*	=	SST model coefficient (0.09)
γ	=	ratio of specific heats
Δx, Δy, Δz	=	local grid distance increments
ε	=	turbulent dissipation
$\varepsilon_{\mathrm{RANS}}$	=	RANS turbulent dissipation
Λ	=	SST–MS model parameter defined in Eq. (9)
ν_t	=	eddy viscosity
$\nu_{t\mathrm{LES}}$	=	subgrid eddy viscosity
$\nu_{t\mathrm{RANS}}$	=	RANS eddy viscosity
Ω	=	vorticity magnitude
ω	=	specific dissipation

Introduction

SEVERAL investigators[1–3] have noted a limitation with traditional Reynolds-averaged Navier–Stokes (RANS) turbulence models applied to unsteady flows. The RANS turbulence models produce too much eddy viscosity and overdamp the unsteady motion of the fluid. The problem is inherent in the construction of the RANS turbulence models because of the assumption that all scales of the unsteady motion of the fluid are to be captured and modeled by the turbulence model. Spatially filtered turbulence models such as large-eddy Simulation (LES) can provide improved results for simulating unsteady flows. LES models are currently limited to fairly low Reynolds numbers because of the grid sizes required to resolve the small-scale turbulent structures.

One approach to overcoming the shortcomings of RANS and LES models applied to unsteady flows at high Reynolds numbers is to spatially filter the RANS turbulence models so that the eddy viscosity does not include the energy of grid-resolved turbulent scales. The spatially filtered RANS turbulence model may be thought of as an LES-like subgrid model for very large turbulent eddies. Turbulence models of this type have been called hybrid RANS/LES models because they incorporate aspects of both forms of turbulence modeling. These hybrid models maintain their RANS nature in the boundary-layer region and transition to spatially filtered LES-like models away from the body if the grid resolution is sufficiently fine in the region of interest. Hybrid models are applicable to unsteady flows dominated by large-scale turbulent structure occurring outside of the boundary layer. It is desirable that the spatial filter functions chosen not degrade the performance of the turbulence model when the largest turbulent scales present are below the resolution of the grid, as is often the case in current aircraft computational fluid dynamics (CFD) applications.

This new class of turbulence models is inherently grid-size dependent because increasing the grid resolution allows smaller and smaller turbulent scales to be resolved. This is both a strength and a weakness of this approach to turbulent flow simulation. There has been little investigation to date of the accuracy of these models in the transition region between RANS and LES. Different models will follow different paths through this transition region, depending on the function used to determine the subgrid contribution of the turbulence model. The transition function may depend on the local grid spacing alone or may also include some approximation of the local turbulent length scale. Though hybrid models do not include an explicit dependency on time step, a sensitivity may exist if the time step selected is much larger than the turbulent timescales of the grid-resolved flow structure. The user must be aware of the relevant turbulent scales when developing grid systems and choosing time steps to allow the appropriate turbulent scales to be captured in the simulation.

This paper applies three of these new hybrid models to two generic test problems, a circular cylinder at high Reynolds number and a rectangular weapons bay. The circular cylinder represents a class of unsteady flow problems in which the separation point on the body is not fixed to a particular point due to the geometry of the body.

Received 7 April 2005; revision received 2 August 2005; accepted for publication 17 August 2005.

*Research Associate Professor, Department of Mechanical Engineering. Senior Member AIAA.

This class of problem is representative of the flows encountered in high-angle-of-attack aerodynamics. The rectangular bay case represents unsteady flows that have a fixed separation point due to the geometry of the problem (the leading edge of the cavity in this case). This bay case is of current interest to aircraft weapons integration designers.

Several investigators have looked at the subsonic vortex shedding from a circular cylinder, but most of the work has been limited to lower Reynolds numbers than are addressed in the present study. Travin et al.[4] evaluated one hybrid RANS/LES model for Reynolds numbers ranging from 1.4×10^4 to 3.0×10^6 using a fifth-order spatial upwind LES flow solver. Vatsa and Singer[5] applied the same hybrid RANS/LES model to cylinders with Reynolds numbers from 5×10^4 to 1.5×10^5 using a second-order spatial Navier–Stokes solver. Hansen and Forsythe[6] and Elmiligui et al.[7] applied hybrid RANS/LES models to cylinders at a Reynolds number of 1.5×10^5. Hansen and Forsythe included a grid-refinement study. Turbulent boundary-layer transition location is an issue at the lower Reynolds numbers of most of the studies. At Reynolds numbers above 6×10^6, the boundary-layer transition point has moved upstream to the point that the flow is predominantly or fully turbulent. The distribution of pressure is relatively insensitive to Reynolds number in this range, and the unsteady flow is generally periodic. This work investigates grid and time-step sensitivity for three hybrid RANS/LES turbulence models for the case of a circular cylinder at a Reynolds number of 8×10^6 using a traditional third-order spatial upwind implicit solver.

Researchers have been attempting to predict the acoustical environment inside a weapons bay for several years. The acoustic levels are often large enough to damage the weapons contained within the bay when the bay is opened. The Baldwin–Lomax[8] algebraic turbulence model was used in investigations by Rizzetta,[9] Suhs,[10] and Baysal et al.[11] These applications represent an early form of hybrid turbulence modeling where an algebraic turbulence model was applied to the flat plate outside the bay, but the turbulence model was not used in the shear-layer region of the cavity. This methodology allowed for a reasonable simulation of the incoming boundary layer, which is critical for calculating reasonable time-averaged pressures and overall sound pressure levels. The sound pressure level spectrum was generally overpredicted because the effects of subgrid scale turbulence were not included in the shear layer.

Nichols and Tramel[1] used a two-equation $k-\varepsilon$ turbulence model for a supersonic cavity application. The time-averaged pressure and overall sound pressure were in reasonable agreement with experimental data. The spectral peaks were predicted at the proper frequencies, but the levels were underpredicted. This was because the turbulence model was providing too much eddy viscosity in the cavity shear layer.

Sinha et al.[2] and Arunajatesan et al.[12] investigated a supersonic bay using a hybrid RANS/LES turbulence model. They found time-averaged pressures and overall sound pressure levels to be in reasonable agreement with experimental data. However, the spectral results were not in agreement with the data of Ref. 13. Nichols and Nelson[14] present results for two RANS models and two hybrid RANS/LES models for a transonic bay. In this case, the hybrid RANS/LES results were in good agreement with the data for the time-averaged pressure, overall sound pressure level, and sound pressure level spectrum.

Rizzetta and Visbal[15] used LES to investigate a simple rectangular cavity having a length-to-depth ratio of 5:1. The side walls of the cavity were not included in the simulation. The grid system contained 2×10^7 points for a simulation of $M = 1.19$ flow at a Reynolds number of 2×10^5, based on cavity length. As a reference, a full-scale aircraft bay would have a Reynolds number based on cavity length of greater than 1×10^8. Rizzetta[11] and Visbal ran their simulation for more than 50,000 time steps on 254 processors using a second-order time, fourth-order spatial compact difference algorithm. No wall clock times were provided for the simulation. Although this simulation was useful for understanding the fluid dynamic phenomena of unsteady bay flow, it is presently too computationally expensive to apply to real flight vehicles.

Theory

There are two possibilities for developing hybrid models from existing RANS models. A first approach would be to modify the production or dissipation source terms in the turbulence model differential equations to include additional terms to adjust the local turbulence variables so that they would not include the grid-realized contribution. This means that the turbulence quantities normally transported by the RANS turbulence model would be created or destroyed on the basis of the local grid resolution.

A second approach would be to solve the existing RANS turbulence model in the normal manner and then filter the results to determine the level of eddy viscosity that will be used in the solution of the Navier–Stokes equations. This approach is somewhat simpler to develop because it requires no tuning of the differential transport equations and can be easily extended to different RANS turbulence models.

Spalart–Allmaras DES Model

Both approaches have been applied to unsteady flows. One example of the first form of a hybrid RANS/LES turbulence model based on the Spalart–Allmaras (SA) one-equation turbulence model[16] can be found in Ref. 3. The standard SA turbulence model contains a destruction term for eddy viscosity that is inversely proportional to the square of the distance from the wall, d. Spalart et al.[3] suggest replacing the wall distance d in the destruction term with

$$\tilde{d} = \min(d, C_{\mathrm{DES}} L_g) \tag{1}$$

where C_{DES} is a constant of $\mathcal{O}(1)$ (normally taken as 0.65) and L_g is a grid length scale defined by

$$L_g = \max(\Delta x, \Delta y, \Delta z) \tag{2}$$

where Δx, Δy, and Δz are the local grid lengths. The modified destruction term has the effect of decreasing the eddy viscosity in regions of tight grid spacing. This modification causes the SA RANS turbulence model to behave like a Smagorinsky LES turbulence model when the grid spacing L_g is less than the distance from the wall, which is generally the case outside of the boundary layer. Note that the transition from RANS to LES does not include any turbulent length-scale dependence, but is solely a function of the local grid spacing. Spalart et al.[3] introduced the term detached-eddy simulation (DES) to describe this model. This hybrid model will be referred to as the SA–DES model. SA–DES has been applied to a number of unsteady flow problems including flow over a sphere,[17] flow over a delta wing,[18] and flow over an aircraft.[19] This model was used in the cylinder studies of Refs. 4–6.

Shear Stress Transport–DES Model

Strelets[20] gives a similar modification to Menter's shear stress transport (SST) two-equation model (see Ref. 21). This hybrid model will be referred to as SST–DES. In this hybrid model, the dissipation term ε in the turbulent kinetic energy equation k is replaced by

$$\varepsilon = \beta^* k\omega = k^{\frac{3}{2}} / \min(L_t, C_{\mathrm{DES}} L_g) = \varepsilon / \min[1.0, C_{\mathrm{DES}}(L_g / L_t)] \tag{3}$$

where

$$L_t = \sqrt{k} / \beta^* \omega = k^{\frac{3}{2}} \Big/ \varepsilon \tag{4}$$

$$C_{\mathrm{DES}} = (1 - F_1) C_{\mathrm{DES}KE} + F_1 C_{\mathrm{DES}KW} \tag{5}$$

Here $\beta^* = 0.09$, $C_{\mathrm{DES}KE} = 0.61$, and $C_{\mathrm{DES}KW} = 0.78$. The function F_1 is the SST turbulence model switching function. The turbulent dissipation ε defined in Eq. (3) is effectively increased when the grid size length scale L_g is less than the turbulent length scale L_t. This causes the turbulent kinetic energy k, and hence the eddy viscosity,

to be reduced in these regions. Unlike the one-equation SA–DES model, this model does include a dependency on the local turbulent length scale. The turbulent length scale used in this model is a function of the filtered turbulent quantities. This model behaves like a k–equation LES subgrid model when the turbulent length scale is greater than the grid length scale. The dissipation equation becomes decoupled from the kinetic energy equation in this region because the turbulent dissipation in the k equation is given by an algebraic relationship given in Eq. (3).

SST–Multiscale Model

Nichols and Nelson[14] give an example of the second approach for developing a hybrid RANS/LES turbulence model, which they have designated a multiscale model (MS). The method was implemented in conjunction with the SST two-equation turbulence model (SST–MS). The SST model is solved using unfiltered turbulence quantities, and the resulting eddy viscosity is filtered and passed to the Navier–Stokes solver. The RANS subscript denotes unfiltered quantities, and the subscript LES is used to denote subgrid quantities. The turbulent length scale used in this effort is defined by the relation

$$L_t = \max\left(6.0\sqrt{\nu_{t\text{RANS}}/\Omega},\, k_{\text{RANS}}^{\frac{3}{2}}/\varepsilon_{\text{RANS}}\right) \tag{6}$$

where $\nu_{t\text{RANS}}$ is the unfiltered eddy viscosity and Ω is the local mean flow vorticity. This length scale is a mixture of the traditional turbulent-scale definition for two-equation turbulence models ($k_{\text{RANS}}^{3/2}/\varepsilon_{\text{RANS}}$) and the definition usually associated with algebraic turbulence models [$(\nu_{t\text{RANS}}/\Omega)^{1/2}$]. The turbulent length-scale definition could be easily adapted to other types of turbulence models. The subgrid turbulent kinetic energy is defined as

$$k_{\text{LES}} = k_{\text{RANS}} f_d \tag{7}$$

The damping function is defined as

$$f_d = \{1 + \tanh[2\pi(\Lambda - 0.5)]\}/2 \tag{8}$$

where

$$\Lambda = 1.0/\left[1.0 + (L_t/L_g)^{\frac{4}{3}}\right] \tag{9}$$

and where L_g is defined in Eq. (2). The eddy viscosity is then calculated from

$$\nu_t = \nu_{t\text{RANS}} f_d + (1 - f_d)\nu_{t\text{LES}} \tag{10}$$

The LES-based subgrid eddy viscosity is given by

$$\nu_{t\text{LES}} = \min\left(0.0854 L_g \sqrt{k_{\text{LES}}},\, \nu_{t\text{RANS}}\right) \tag{11}$$

The multiscale hybrid model behaves like a traditional SST model on the RANS end of the spectrum and transitions to a nonlinear k-equation model on the LES end of the spectrum. The switching function f_d in Eq. (10) was chosen to allow a smooth transition from the standard RANS turbulence model to the LES subgrid model. This hybrid RANS/LES approach can easily be extended to other RANS turbulence models with little to no alteration providing that a length scale can be derived for that model and a value for the turbulent kinetic energy can be approximated by that model. The multiscale hybrid model, like the SST–DES model, transitions from RANS to LES as a function of the ratio of the local turbulent length scale predicted by the RANS model to the local grid spacing rather than being a function of the grid spacing alone, as is the case for the SA–DES model.

Nelson and Nichols[22] evaluated the SA–DES and the SST–MS hybrid turbulence models as subgrid turbulence models for LES applications. The hybrid models were applied to a high-speed shear layer using a true LES flow solver. The study also included a number of traditional LES turbulence models. The results indicate that these two hybrid models perform as well as more complicated LES subgrid models for the shear-layer application.

Results

Three hybrid RANS/LES turbulence models will be applied to the prediction of the unsteady flow over a circular cylinder at high Reynolds number and for a generic weapons bay configuration. Grid and time-step studies will be conducted for each of the test cases. These calculations will be used to evaluate the performance of the individual models and also to derive some rules-of-thumb for choosing time steps and grid spacings for these problems.

All of the calculations were performed with the NXAIR[23] overset structured implicit flow solver using a second-order time, third-order upwind HHLEM[24] space algorithm. Three Newton subiterations were used to provide local convergence at each time step. A symmetric successive overrelaxation procedure was used to solve the unfactored solution matrix. The turbulence transport equations were solved in a time-accurate manner using a second-order time, second-order upwind space algorithm. The turbulence equations were solved loosely coupled with the mean flow equations within the Newton subiteration loop. The accuracy of NXAIR for unsteady flow applications is discussed in Ref. 25. The wall function boundary conditions of Nichols and Nelson[26] were used in these calculations.

Convergence Criteria and Computational Error Estimation

Numerical convergence must be evaluated in a statistical sense for these unsteady flow simulations. Here it is assumed that demonstrating that a solution is statistically stationary is a sufficient condition for demonstrating convergence. The unsteady computational output is evaluated using overlapping data windows, as shown in Fig. 1. Four windows of 2048 samples are used in this example of a simulated wall pressure. The windows are overlapped because of the limited number of samples available. The windows overlap was chosen as 50% in this study. Although a 50% overlap may be considered high, it should be sufficient to define whether the flow is statistically stationary if more than two windows are used because at least two of the windows are completely independent of each other. The average pressure, overall sound pressure level (OASPL), peak sound pressure level (SPL), and the frequency at which the peak SPL occurred are presented in Table 1. The statistical quantities (mean, rms, and spectral) computed from each window can be used to evaluate the level of convergence and to estimate the

Table 1 Unsteady pressure convergence analysis

Sampling window	Average pressure (P/P_{inf})	OASPL, dB	Peak SPL, dB	Frequency of peak SPL, Hz
1	1.02447	171.392	171.550	48.577
2	1.02412	170.745	170.952	48.577
3	1.01888	170.929	169.526	48.577
4	1.02000	171.027	171.177	48.577
Average	1.02187	171.023	170.801	48.577
Maximum error, %	0.29	0.22	0.747	0.0

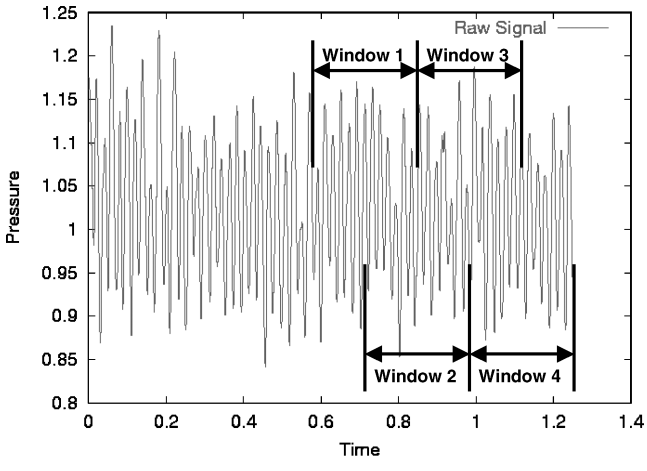

Fig. 1 Example CFD pressure output.

error of the calculation. The computational error is defined as the maximum difference of the individual window statistical quantities from the mean of the quantities for all of the windows divided by the mean of the quantities. Table 1 also includes the computational error for the example case. This result shows deviations of less than 1% and is deemed to be statistically stationary for all of the quantities examined. The SPL spectrum for each window and the average for all of the windows are shown in Fig. 2. The averaging process produces a smoother spectrum than the individual window results. This windowing process was used in all of the spectral examples in this work.

Circular Cylinder

Unsteady three-dimensional calculations were performed for the vortex shedding from a circular cylinder for $M = 0.2$ and $Re_d = 8 \times 10^6$. Three computational grids were used in the simulation: fine, $401 \times 201 \times 201$; mid, $201 \times 101 \times 101$; and coarse, $101 \times 51 \times 51$.

The midlevel and coarse-level grids were constructed by removing every other point from the fine-level and midlevel grids, respectively. The grids have a span of 10 cylinder diameters. Periodic boundary conditions were applied at the side planes of the grid. The initial wall spacing was 2×10^{-4} diameters for the fine-level grid, which corresponds to a $y+$ of about 20. The centerline plane of the three grids is shown in Fig. 3.

The calculations were run 10,500 iterations, and the final 4096 time steps were statistically analyzed. All of the computational spectral results presented here were computed using three overlapping windows of 2048 samples each. The total computational time analyzed was 0.37 s, and the time length for each window was 0.185 s. This represents about 11 cycles of the predominant 60-Hz frequency in each window.

Calculations with three different time steps were run on the midlevel grid with the multiscale hybrid turbulence model to determine an acceptable time step for this simulation. The results are shown in Fig. 4. The primary shedding frequency for this sample is just less than 60 Hz. These solutions correspond to 50 ($\Delta t = 3.6 \times 10^{-4}$ s), 200 ($\Delta t = 9.0 \times 10^{-5}$ s), and 800 ($\Delta t = 2.25 \times 10^{-5}$ s) time steps per shedding cycle. The results from the largest time step are quite different from the smaller time-step results. The spectral peak predicted with the large time step occurs at a much lower frequency than the peak predicted using the smaller time steps. On the basis of these results, all subsequent simulations were performed using the 9.0×10^{-5} s time step with 200 time steps per shedding cycle.

The data in Ref. 27 were obtained using both air ($\gamma = 1.4$) and freon ($\gamma = 1.13$) as a test medium. Freon was used to obtain higher Reynolds numbers at lower Mach numbers in this experiment. Calculations were performed on the midlevel grid with the SST–MS hybrid model to assess the effect of test medium. The predicted average drag coefficient for air was 0.55 and for freon was 0.56. The predicted Strouhal number of the primary lift peak was 0.269 for both air and freon. The normal-force spectral results are shown in Fig. 5. These results indicate that the test medium is not an important factor at the flow conditions of this study. All subsequent solutions were performed using air as the test medium.

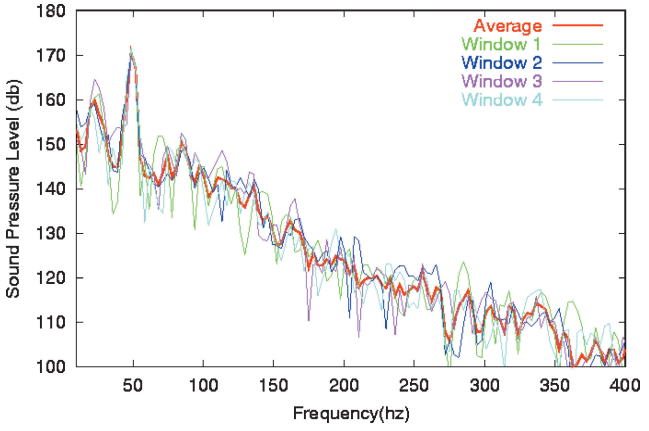

Fig. 2 Individual data windows and averaged sound pressure spectral example.

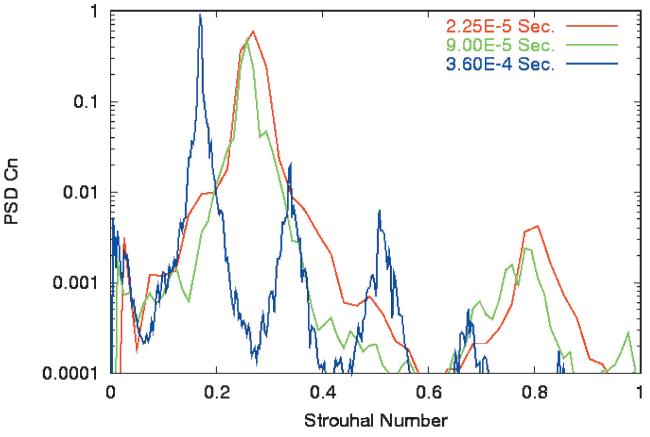

Fig. 4 Normal-force PSD for three different time steps for cylinder.

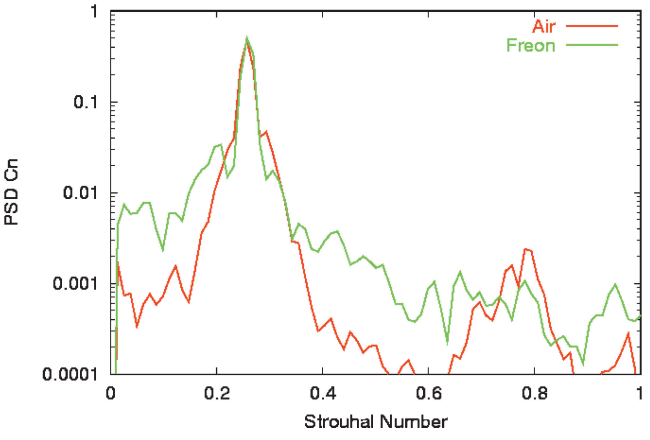

Fig. 5 Normal-force PSD for air and freon, SST–MS hybrid model for cylinder.

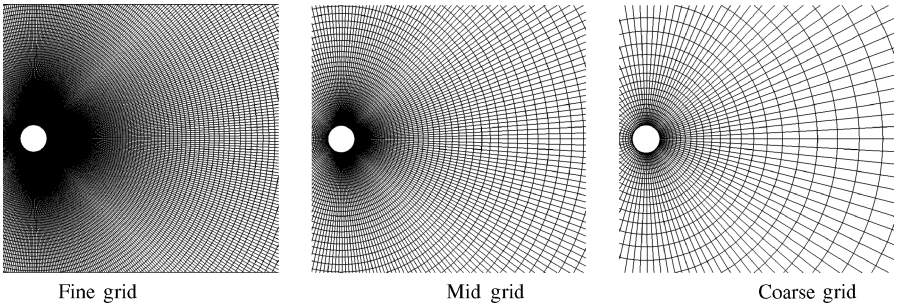

Fig. 3 Cylinder grid centerline.

A comparison of the normal-force power spectral density for the three hybrid models, the SA–RANS model, and the SST–RANS model for the midlevel grid is shown in Fig. 6. The hybrid models show similar trends in that they all have a rather broad spectral peak at a Strouhal number of about 0.25. The two RANS models also have a much narrower spectral peak at a similar Strouhal number. The RANS models have much lower energy away from the peak. This is an indication that the RANS models are providing too much damping of the unsteady solutions.

Instantaneous contour plots are presented in Figs. 7–14. Although the same computational time step was used for all of these plots, the plots do not represent the same point in the shedding cycle because each model develops the unsteady flow process differently. This unsteady development process was seen to be different for the same model on different grid densities. Figures 7–14 are representative of the behavior of the models observed at other time steps.

Instantaneous x vorticity isosurfaces computed with the SST–DES hybrid turbulence model are shown in Fig. 7 for all three grids. The turbulent structure in the wake of the cylinder is clearly evident in the fine-level grid solution. The turbulent structure is reduced in the midlevel grid solution. There is very little structure present in the coarse-level grid solution, and the structure that does exist near the cylinder seems to be nearly two dimensional.

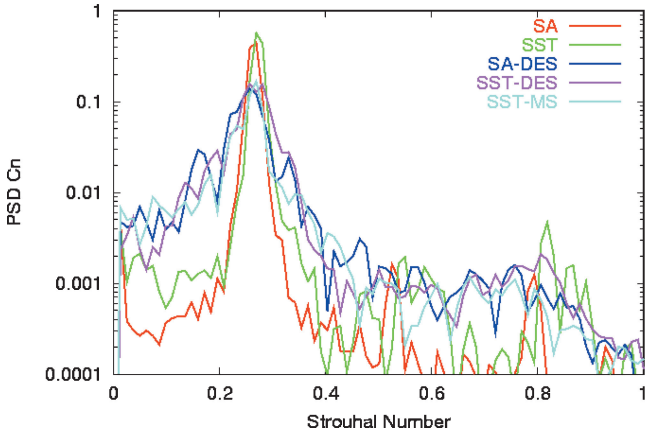

Fig. 6 Normal-force PSD on the midlevel cylinder grid.

Instantaneous contours of Mach number and eddy viscosity for the SA–DES, SST–DES, and SST-MS hybrid turbulence models computed on the three grid levels are shown in Figs. 8–13. All three hybrid turbulence models have similar trends on the three grid levels. Significant turbulent structure can be seen in the fine-level grid solutions with both large- and small-scale turbulent structure present. The midlevel solutions have large-scale structure present, but the smaller turbulent scales are absent. The midlevel grids also have structure that appears to be more periodic than does the fine-level grid solution. The coarse-level solutions show almost no turbulent structure and produce an almost steady-state wake away from the cylinder. The level of eddy viscosity in the wake differs for the three turbulent models. The eddy viscosity for the SA–DES model shown in Fig. 9 indicates that this model effectively shuts off the eddy viscosity outside the boundary layer. The eddy viscosity for the SST–DES and the SST–MS models is reduced as the grid is refined. The SST–DES model tends to predict higher levels of eddy viscosity in the wake region than does the SST–MS model. The SST–DES model also predicts higher eddy viscosities along the edges of the wake than either the SA–DES or SST–MS models. Both the SST–DES and SST–MS models are tending toward a RANS-type solution in the far wake of the coarse-level grid solution.

The ratio of the turbulent length scale to the local grid length scale for the SST–MS model is shown in Fig. 14 for the three grid levels. The length-scale ratio seems to scale with the grid refinement for the midlevel to fine-level grid results, indicating that the turbulent length scales predicted on the midlevel and fine-level grids are similar. The midlevel grid results in a length-scale ratio of greater than two for most of the wake region. The coarse-level grid results indicate that the hybrid model is operating in the RANS mode.

The power spectral densities (PSD) of the axial normal-force coefficient are shown in Figs. 15–17 for the three hybrid turbulence models. The spectral bin size is 5 Hz ($\Delta Sr = 0.024$). The midlevel and fine-level grid results are in general agreement to within the spectral resolution of the fast Fourier transform (FFT) for all three hybrid turbulence models. The coarse-level grid solutions are seen

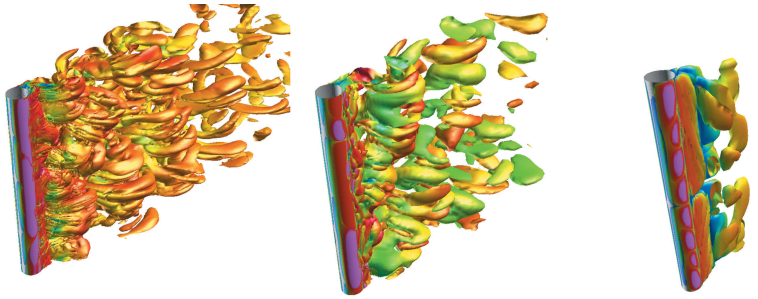

Fig. 7 Instantaneous vorticity isosurfaces colored by Mach number for SST–DES hybrid turbulence model on cylinder.

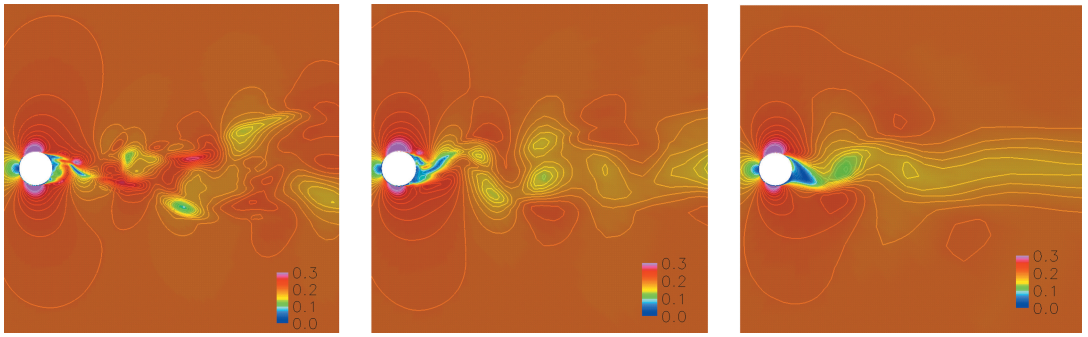

a) Fine **b) Mid** **c) Coarse**

Fig. 8 Instantaneous Mach number contours for SA–DES hybrid turbulence model applied to cylinder.

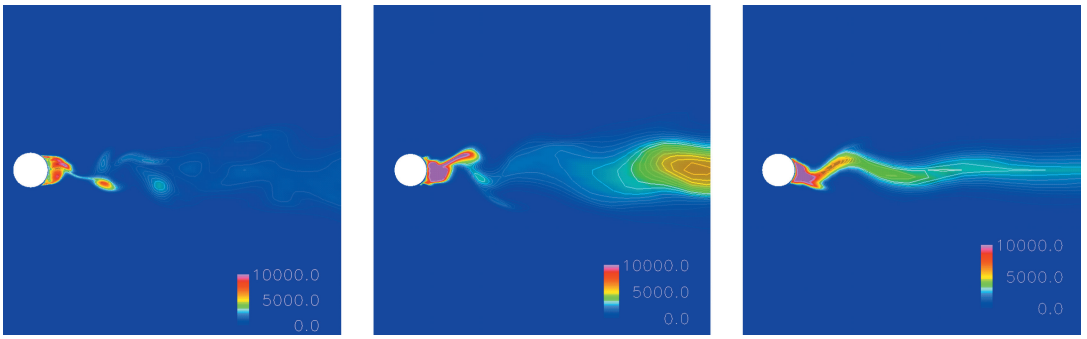

a) Fine b) Mid c) Coarse

Fig. 9 Instantaneous eddy-viscosity contours for SA–DES hybrid turbulence model applied to cylinder.

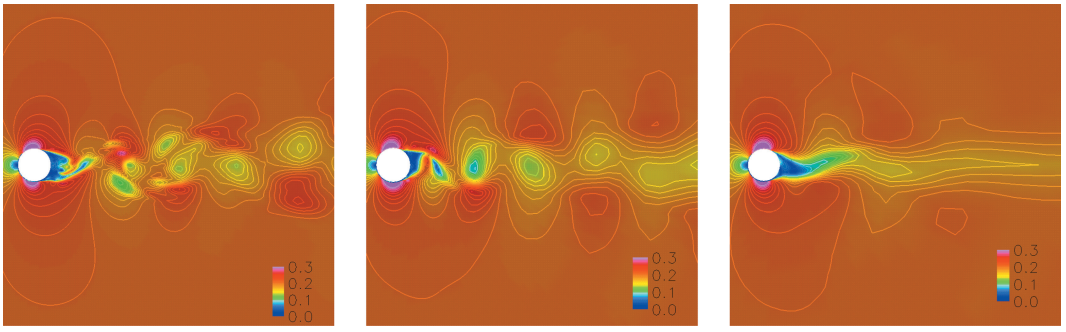

a) Fine b) Mid c) Coarse

Fig. 10 Instantaneous Mach number contours for SST–DES hybrid turbulence model applied to cylinder.

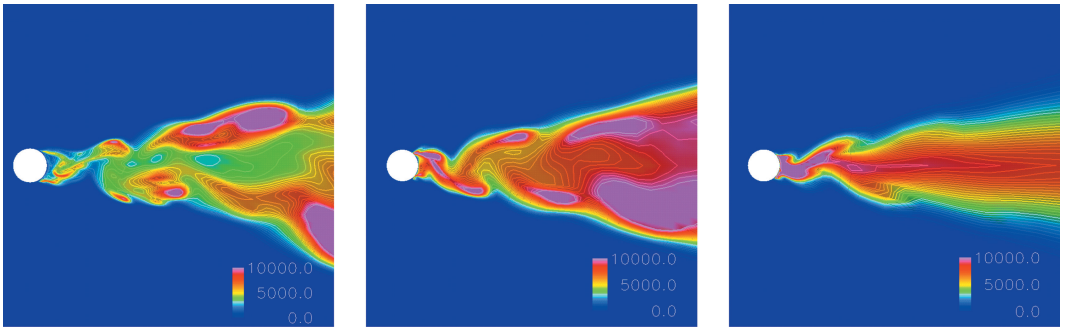

a) Fine b) Mid c) Coarse

Fig. 11 Instantaneous eddy-viscosity contours for SST–DES hybrid turbulence model applied to cylinder.

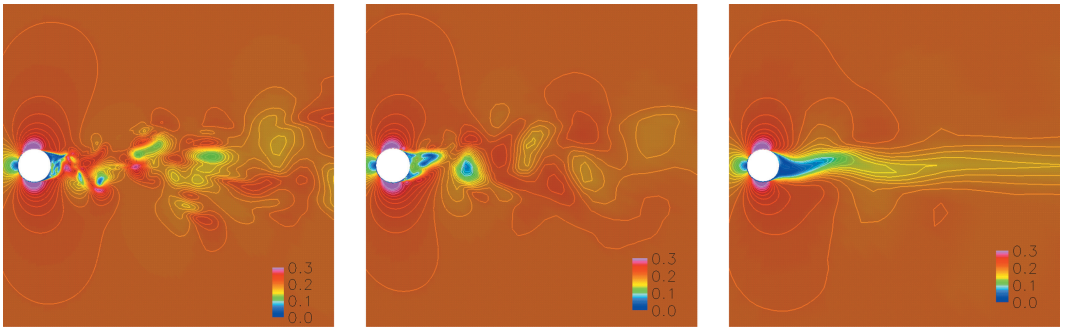

a) Fine b) Mid c) Coarse

Fig. 12 Instantaneous Mach number contours for SST–MS hybrid turbulence model applied to cylinder.

to be significantly different, and the energy is contained in narrower peaks for all of the hybrid models. The coarse-level grid solutions are similar to the traditional RANS turbulence model results shown in Fig. 6, indicating that the hybrid models are operating in the RANS mode for most of the flow.

The average integrated drag coefficient C_d and the peak lift coefficient Strouhal number Sr for the three hybrid models computed on the three grid levels are shown along with experimental results[27–29] in Table 2. The experimental results were obtained in wind tunnels with a blockage of 18.75% (cylinder diameter/tunnel height) in Ref. 27 and 13.6% in Ref. 28. These blockage levels are quite large. Roshko[28] presents a blockage correction for the drag of the cylinder based on image doublets. The correction is given by

$$C_{d\text{corrected}} = C_{d\text{measured}}\left[1 - 0.5(d/h)C_{d\text{measured}} - 2.5(d/h)^2\right] \quad (12)$$

where d is the cylinder diameter and h is the tunnel height. This results in an approximate correction of greater than 10% for both Refs. 27 and 28. The Ref. 28 data include this correction, whereas

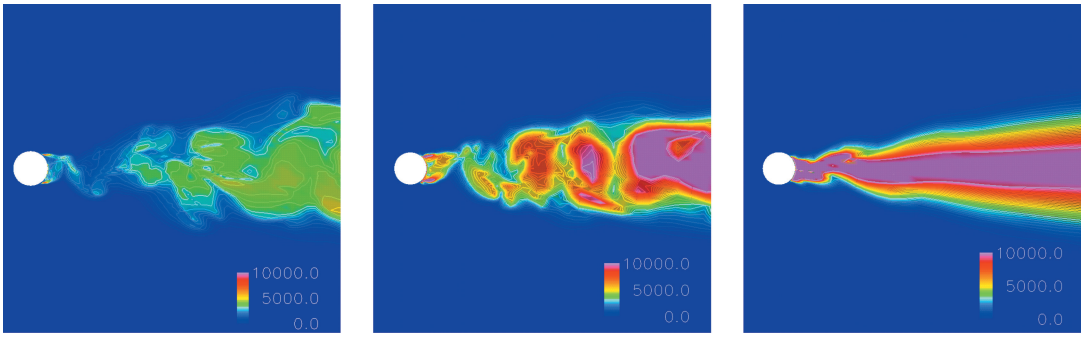

a) Fine b) Mid c) Coarse

Fig. 13 Instantaneous eddy-viscosity contours for SST–MS hybrid turbulence model applied to cylinder.

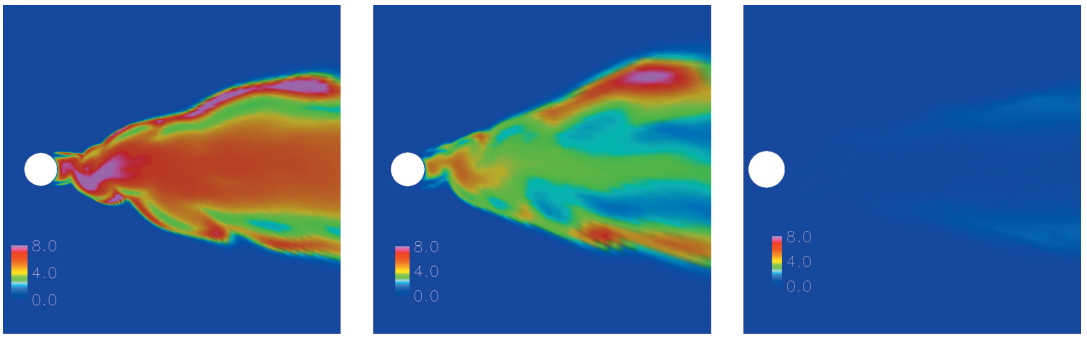

a) Fine b) Mid c) Coarse

Fig. 14 Instantaneous ratio of turbulent length scale to grid length scale, SST–MS hybrid turbulence model applied to the cylinder.

Table 2 Force coefficient and Strouhal number predictions on the three-dimensional circular cylinder

Model	Grid	Average C_d	CFD C_d error, %	Sr
SA	Coarse	0.27	5.5	0.220
SST	Coarse	0.19	0	0.232
SA–DES	Coarse	0.30	0.5	0.220
SST–DES	Coarse	0.22	0.2	0.232
SST–MS	Coarse	0.20	0	0.232
SA	Mid	0.51	0.1	0.269
SST	Mid	0.52	0	0.269
SA–DES	Mid	0.63	1.5	0.256
SST–DES	Mid	0.59	1.0	0.256
SST–MS	Mid	0.55	3.4	0.269
SA–DES	Fine	0.52	2.3	0.244
SST–DES	Fine	0.59	7.9	0.244
SST–MS	Fine	0.58	3.3	0.256
DATA[27]		0.51–0.54	——	0.31
DATA[28]		0.79	——	0.27
DATA[29]		——	——	0.29
SA–DES[4]		0.41–0.51	——	0.33–0.35

the Ref. 27 data do not. The Ref. 27 data presented were obtained at a freestream Mach number of 0.2, whereas the Ref. 28 data were obtained at a freestream Mach number of 0.25. Data obtained in Ref. 27 at a freestream Mach number of 0.25 indicate the drag coefficient should be approximately 0.05 higher at this Reynolds number than the drag coefficient at a freestream Mach number of 0.2. The drag rise is attributable to the onset of compressibility effects that begin above a freestream Mach number of 0.2 (Ref. 27). The combination of blockage and compressibility effects may account for the large scatter in the experimental drag coefficient. The experimental Strouhal number does not seem to be as sensitive as drag coefficient to blockage and compressibility.

The midlevel and fine-level grid drag coefficient results are in general agreement with the Ref. 27 experimental data and with the computational results of Travin et al.[4] obtained at a Reynolds number of 3.0×10^6. The Strouhal number predictions are consistently

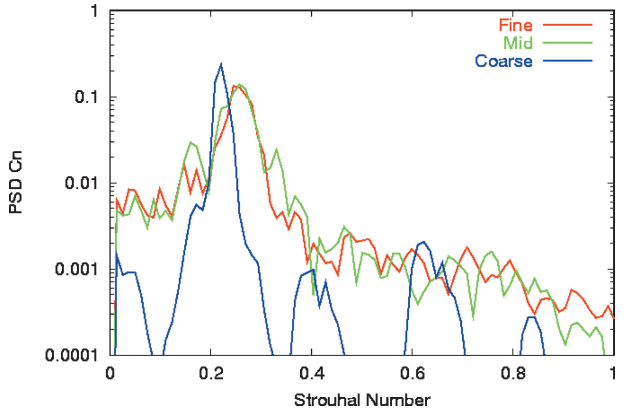

Fig. 15 Power spectral density of normal-force coefficient for SA–DES hybrid model for the cylinder.

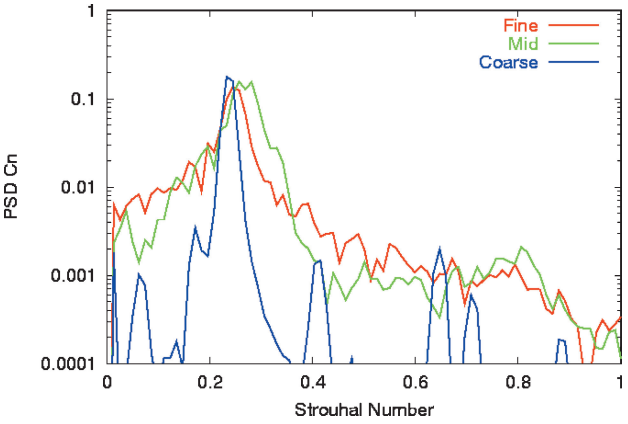

Fig. 16 PSD of normal-force coefficient for SST–DES hybrid model for the cylinder.

Table 3 Grid refinement study error relative to the fine grid for the circular cylinder

Model	Grid	Difference in average C_d, %	Difference in Sr, %
SA–DES	Coarse	52.4	9.8
SST–DES	Coarse	62.7	4.9
SST–MS	Coarse	65.5	9.4
SA–DES	Mid	21.2	4.9
SST–DES	Mid	0	4.9
SST–MS	Mid	5.2	5.1

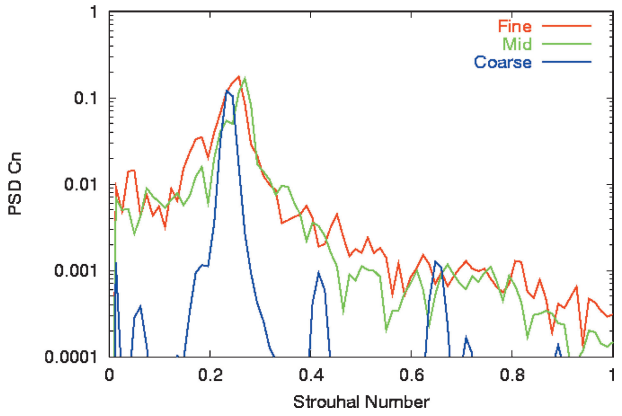

Fig. 17 PSD of normal-force coefficient for SST–MS hybrid model for the cylinder.

lower than the experimental data. The coarse-level grid results for the hybrid models are in relative agreement with the RANS models on which they are based, indicating that the hybrid models are operating in RANS mode on this grid level. The hybrid model results differ significantly from the RANS models on the midlevel grid. This indicates that the transition from RANS to LES occurs rapidly with grid spacing variation for all three of the hybrid models tested.

An estimate of the computational error caused by the limited number of samples used in the computations of the average drag coefficient is also included in Table 2. This error was computed by using the windowing method described earlier, that is, taking the maximum difference between the individual windows and the mean of the windows, with three overlapping windows of 2048 samples each. The error in the average drag is seen to increase with increasing grid refinement for all three models. This error increase may be caused by the additional turbulent scales that are present on the finer grids and could possibly be reduced by longer sampling times, that is, running more time steps.

The percentage difference of the average drag coefficient and the Strouhal number relative to the fine-grid solution are shown in Table 3. The grid refinement study did produce convergence in the predicted Strouhal number to within the frequency resolution of the FFT ($\Delta Sr = 0.024$). The average drag for the SST-based hybrid models also reaches convergence within the error shown in Table 2. The SA–DES hybrid model average drag does not reach convergence on the grid levels tested here. The grid-refinement study performed using the SA–DES model described in Ref. 6 also failed to produce grid convergence. The coarse-level grid is inadequate for all of the hybrid RANS/LES models tested.

WICS Bay

Unsteady Navier–Stokes calculations were performed for the Weapons Internal Carriage and Separation (WICS) $L/D = 4.5$ weapons bay[13] for $M = 0.95$ and $Re = 7.6 \times 10^5$/m. The wind-tunnel data were obtained in the Arnold Engineering Development Center (AEDC) 4-ft transonic wind tunnel. The weapons bay was 18 in. long, 4 in. wide, and 4 in. deep. The bay has a length-to-depth ratio of 4.5 and is considered a deep bay. (The shear layer does not attach to the ceiling of the bay.) The bay was located behind a 15-in. flat plate in the experimental configuration.

The computational geometry was a flat plate that extended 15 in. upstream of the bay, to match the experiment, and 25 in. downstream of the bay. The sides of the computational grid extended 50 in. on either side of the bay centerline. The full bay geometry was modeled using wall functions. The wall spacing was chosen as 0.0075 in., which corresponds to a $y+$ of 50 on the upstream plate. The wall spacing inside the bay was set to 0.075 in. The larger wall spacing may be used inside the bay because the wall shear stress is much lower there. These wall spacings were used for all of the grids in the grid-refinement study. The boundary-layer height on the flat plate just upstream of the cavity was found to be 0.25 in. for both the experiment and the computations.

The calculations were run 10,500 iterations, and the final 8192 time steps were statistically analyzed. The computational spectral results presented here were computed using three overlapping windows of 4096 samples each. The total computational time analyzed was 0.13 s and the time length for each window was 0.065 s. This represents about 30 cycles of the predominant 465-Hz frequency in each window. The computational OASPL error, that is, the maximum difference between the individual windows and the mean of the windows, was found to be less than 1 dB for all of the models on all of the grids.

Grid-resolution effects were investigated by modifying the bay grid and the grids in the vicinity of the bay grid. The grids upstream and to the sides of the bay were not modified. Details of the grid systems used in this study are shown in Table 4. The centerline plane of the three bay grids is shown in Fig. 18.

A time-step study was performed using the SST–MS hybrid model and the medium-grid set. Time steps of from 8.0×10^{-6} to 8.0×10^{-5} s were evaluated. A time step of 8.0×10^{-6} s corresponds to 260 time steps per cycle for the primary spectral mode of the cavity at 450 Hz. The results are compared to data[24] for the K16 and K18 transducer locations in the bay in Figs. 19a and 19b, respectively. K16 is located on the bay ceiling centerline, 0.275 in. from the back wall. K18 is located on the bay back wall centerline, 0.725 in. from the bay opening. The K18 transducer is in a more dynamic region of the flow because of its proximity to the shear layer above the bay. The agreement with the measured spectra is seen to improve at the higher frequencies as the time step is reduced. The solution with the largest time step predicts the primary spectral peaks at too low a frequency.

A summary of the spectral peak predictions at the K18 locations is given in Table 5. Because frequency of the pressure oscillation increases at a given time step, the solution will eventually

Table 4 Parameters for grid refinement study for the WICS bay

Grid	Total points	Bay grid dimensions	Bay grid Δx_{max}, in.	Bay grid Δy_{max}, in.	Bay grid Δz_{max}, in.
Fine	1.8×10^6	$121 \times 61 \times 61$	0.3	0.1	0.1
Medium	1.1×10^6	$71 \times 41 \times 41$	0.6	0.2	0.2
Coarse	7.9×10^5	$61 \times 31 \times 31$	0.75	0.3	0.3

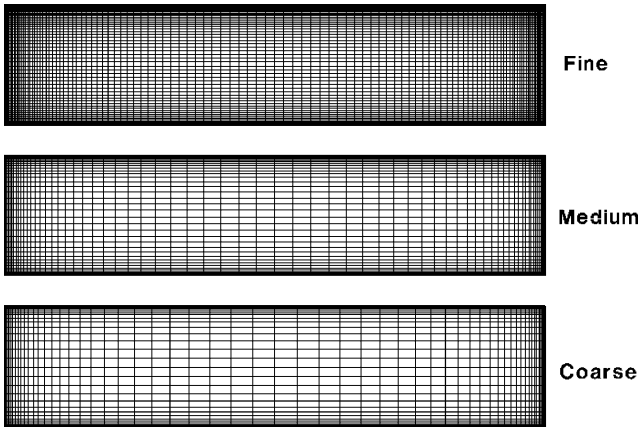

Fig. 18 Centerline plane of WICS bay grids.

Table 5 Effect of time-step size variation on spectral peak prediction for the K18 transducer location

	First peak		Second peak		Third peak		Fourth peak	
Δt, s	Frequency, Hz	SPL	Frequency, Hz	SPL	Frequency, Hz	SPL	Frequency, Hz	SPL
8.0×10^{-5}	198	158	409	168	657	151	——	——
4.0×10^{-5}	198	159	446	168	731	153	942	148
1.6×10^{-5}	201	161	450	165	728	158	1038	154
8.0×10^{-6}	186	164	455	166	728	159	1022	151
Data	195	158	450	165	732	158	1025	150

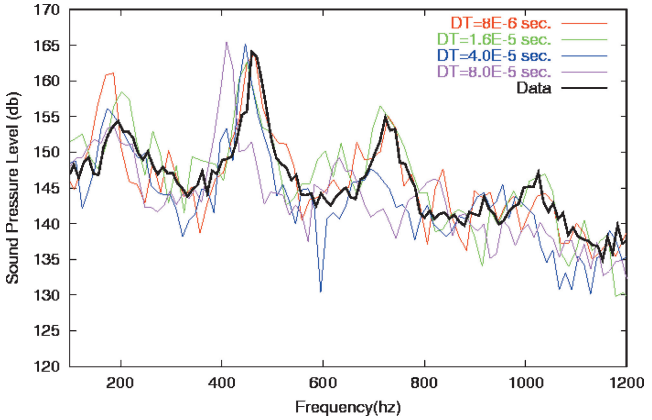

Fig. 19a SPL spectra at WICS K16 (ceiling) location, varying time step.

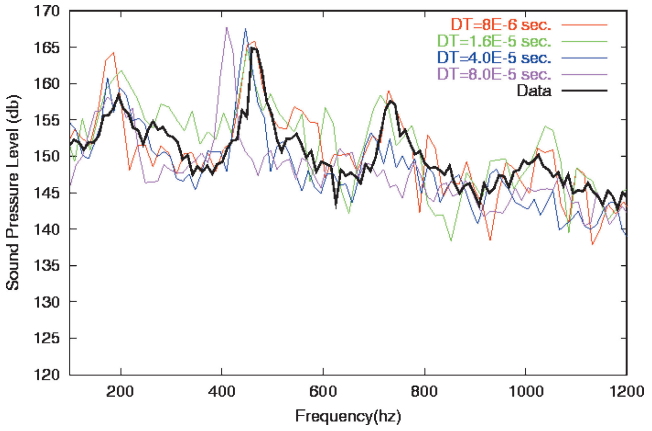

Fig. 19b SPL spectra at WICS K18 (back wall) location, varying time step.

underresolve the flow. As the time step increases, fewer cycles of the low-frequency waves are included in the sampling window. The large time step does a reasonable job of predicting the first peak with about 64 time steps per cycle. The higher frequency peaks are underresolved. The smallest time step does well on the fourth peak with about 120 time steps per cycle, but does not do as well on the first peak with only 13 cycles per window. The solution using 1.6×10^{-5} s time step has reasonable agreement with the first three spectral peaks on the K16 location and the first four peaks at the K18 location. All subsequent solutions were performed using the 1.6×10^{-5} s time step.

Instantaneous contour plots are presented in Figs. 20–26. As in the cylinder computation, the same computational time step was used for Figs. 20–26. Figures 20–26 do not represent the same point in the shedding cycle because each model develops the unsteady flow process differently. This unsteady development process was seen to be different for the same model on different grid densities. Figures 20–26 are representative of the behavior of the models observed at other time steps.

Instantaneous Mach number and eddy-viscosity contours with the three hybrid models on the bay centerline are shown in Figs. 20–25 for all three grids. The turbulent structure shown in the Mach number contours is seen to dramatically increase with grid resolution for all three hybrid models. The shear layer is seen to grow and then burst as it traverses the bay. The eddy viscosity decreases with increasing grid resolution, as is expected for all three hybrid models. The SST–DES hybrid model has the largest levels of eddy viscosity, and the maximum eddy viscosity is located in the shear layer. The ratio of the turbulence length scale to the grid length scale (L_t/L_g) for the SST–MS model is shown in Fig. 26. The contours scale with the grid refinement, as is expected for this model.

Table 6 Comparison of absolute maximum difference relative to fine grid solution in average pressure coefficient and OSPL for WICS bay ceiling

Model	$\Delta C_{p_{\max}}$ Fine–coarse	$\Delta C_{p_{\max}}$ Fine–medium	$\Delta\text{OASPL}_{\max}$ Fine–coarse, dB	$\Delta\text{OASPL}_{\max}$ Fine–medium, dB
SA–DES	0.1143	0.0971	3.94	1.87
SST–DES	0.1049	0.0897	2.99	1.33
SST–MS	0.1567	0.0786	4.30	2.05

The time-averaged pressure coefficient on the bay ceiling is shown in Fig. 27 for the three hybrid models. The SPL on the bay ceiling is shown in Fig. 28. The solutions are similar for the three models for both of these properties. There is some sensitivity to grid density for the average pressure coefficient on the downstream end of the ceiling. The coarse- and fine-grid solutions are quite similar for both the time-averaged pressure coefficient and the SPL for all three models tested. The medium-grid solutions are bracketed by the coarse and fine solutions. The medium-grid solutions for pressure coefficient for the SA–DES and SST–DES models are in close agreement with the coarse-grid solutions. The medium-grid solution for pressure coefficient for the SST–MS model is approaching the fine-grid solution. The maximum difference in pressure coefficient and OASPL relative to the fine-grid solution for the ceiling is shown in Table 6. The difference is reduced with grid refinement for all three models, indicating that the models are approaching a grid-converged solution. The coarse-grid overall sound pressure is only slightly different from that of the finer grids. This similarity indicates that average pressure coefficient and OASPL are not overly sensitive to grid density for these grid density levels.

The SPL spectra at the K16 and K18 locations for the three hybrid models are shown in Figs. 29–31. The spectral bin size for the computational results was 15 Hz, and the experimental spectral bin size was 10 Hz. The medium- and fine-grid spectra are in reasonable agreement with the first three spectral peaks for the SST-based hybrid models. The two SST-based models provide some resolution of the fourth peak on the medium and fine grids. The coarse-grid spectra are not in as good agreement with the data as the medium- and fine-grid results, but they are not totally unacceptable. The SA–DES model spectra are more sensitive to the grid density than are the SST-based spectra. The frequency and SPL for the primary spectral peak are shown in Table 7. The results show that all of the models on all of the grids predict the frequency of the primary peak within the frequency increment of the Fourier transform (15 Hz) and are also in reasonable agreement with the data. Again the SST-based models are less sensitive to grid density variations than is the SA–DES model.

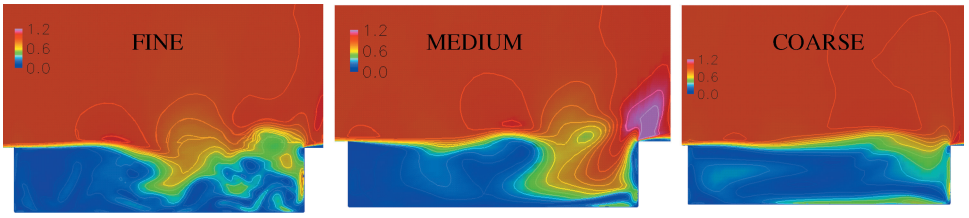

Fig. 20 Instantaneous Mach number contours on bay centerline, SA–DES hybrid model.

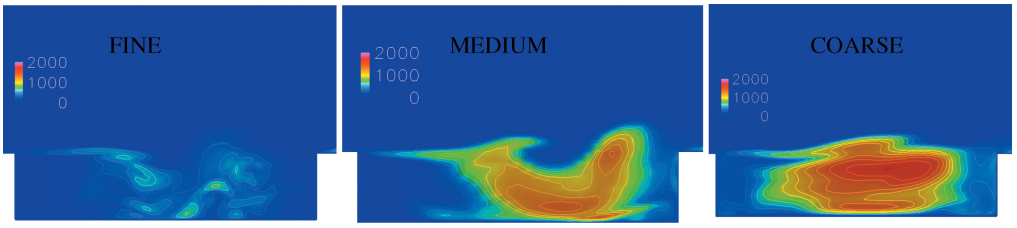

Fig. 21 Instantaneous eddy-viscosity contours on bay centerline, SA–DES hybrid model.

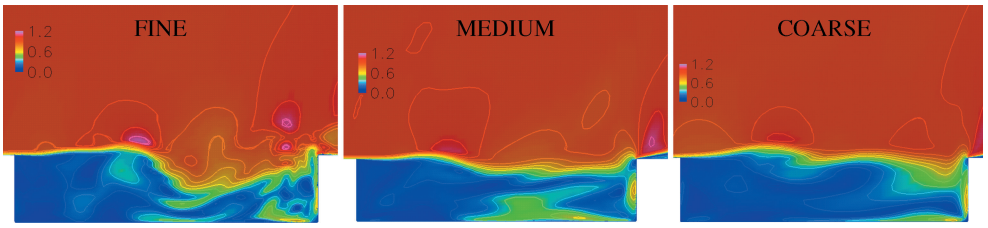

Fig. 22 Instantaneous Mach number contours on bay centerline, SST–DES hybrid model.

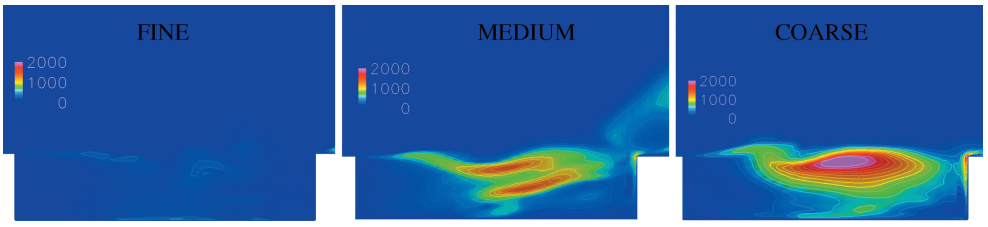

Fig. 23 Instantaneous eddy-viscosity contours on bay centerline, SST–DES hybrid model.

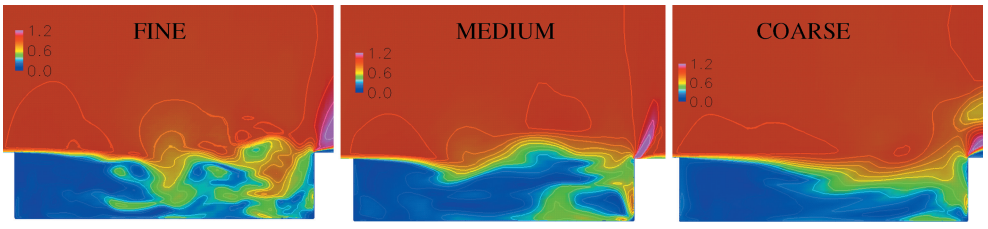

Fig. 24 Instantaneous Mach number contours on bay centerline, SST–MS hybrid model.

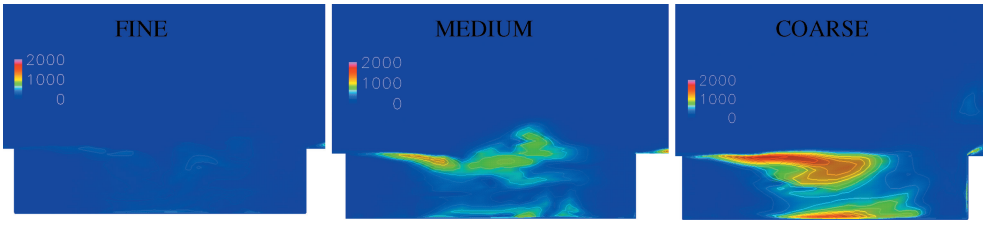

Fig. 25 Instantaneous eddy-viscosity contours on bay centerline, SST–MS hybrid model.

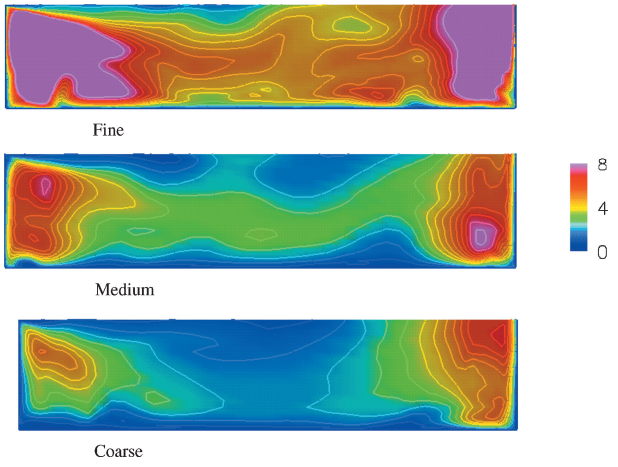

Fig. 26 Instantaneous ratio of turbulent length scale to grid length scale contours on bay centerline, SST–MS hybrid model.

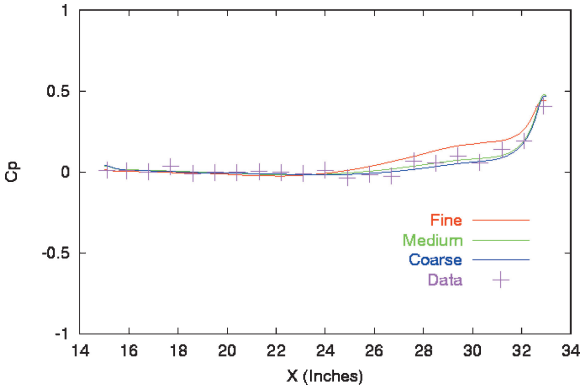

Fig. 27a Average pressure coefficient on WICS ceiling, SA–DES model.

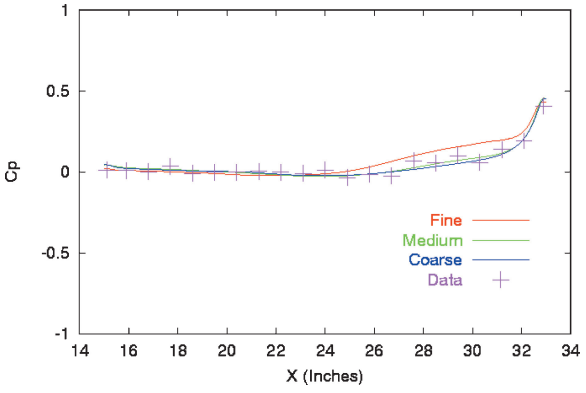

Fig. 27b Average pressure coefficient on WICS ceiling, SST–DES model.

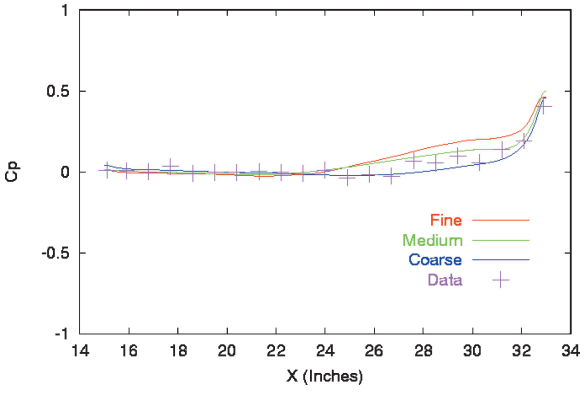

Fig. 27c Average pressure coefficient on WICS ceiling, SST–MS model.

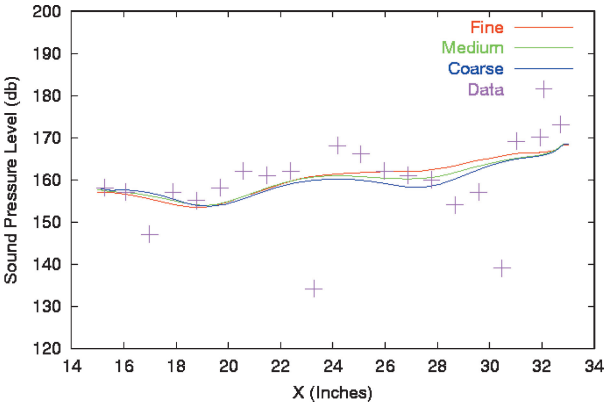

Fig. 28a SPL on WICS ceiling, SA–DES model.

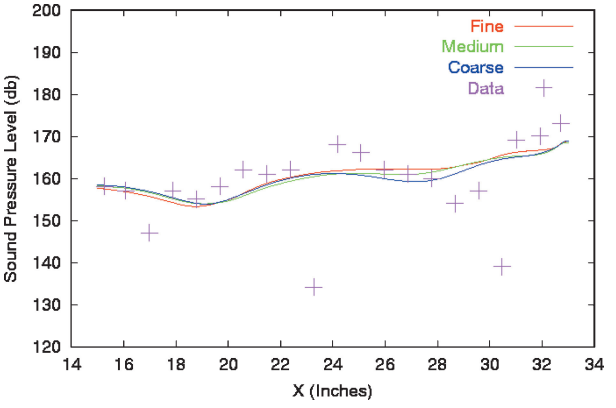

Fig. 28b SPL on WICS ceiling, SST–DES model.

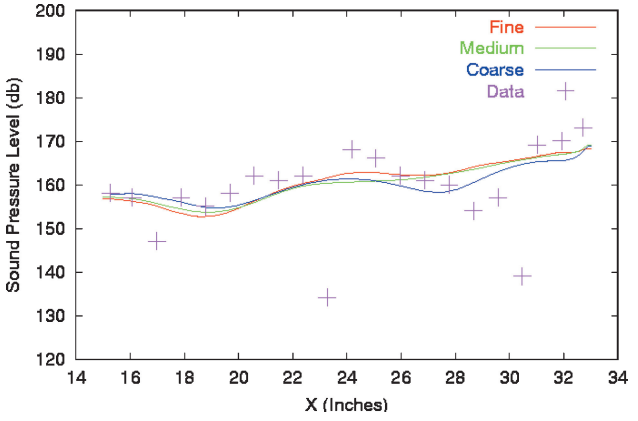

Fig. 28c SPL on WICS ceiling, SST–MS model.

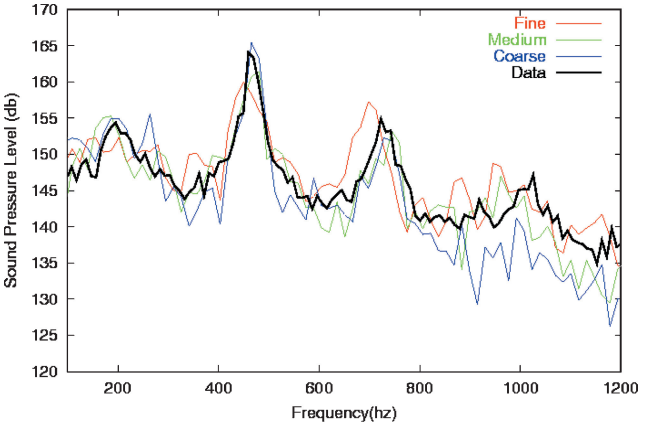

Fig. 29a SPL spectrum at K16 (ceiling) location, SA–DES model.

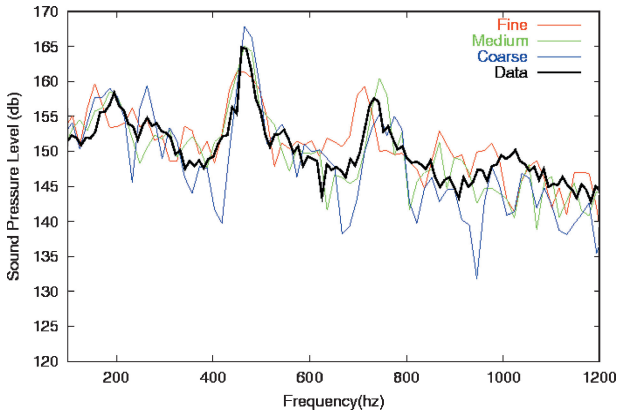

Fig. 29b SPL spectrum at K18 (back wall) location, SA–DES model.

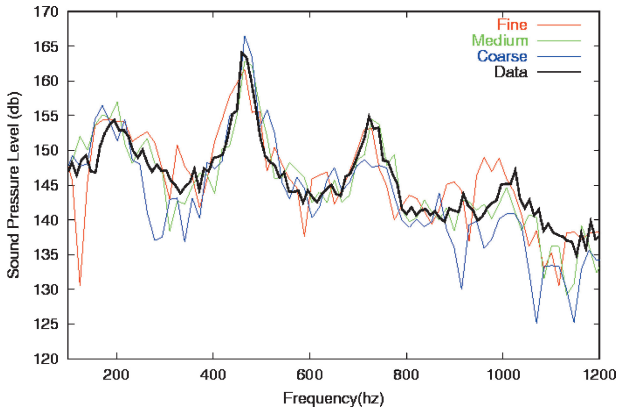

Fig. 30a SPL spectrum at K16 (ceiling) location, SST–DES model.

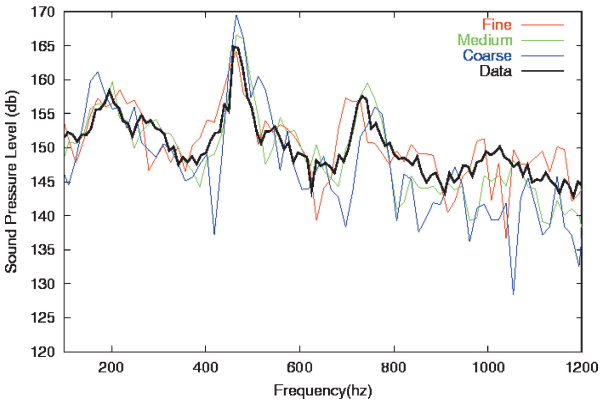

Fig. 30b SPL spectrum at K18 (back wall) location, SST–DES model.

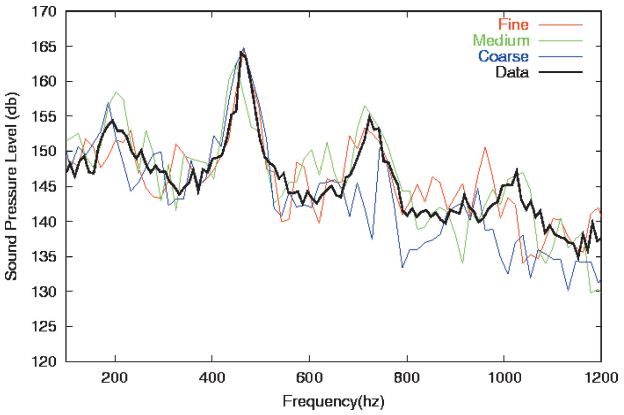

Fig. 31a SPL spectrum at K16 (ceiling) location, SST–MS model.

Table 7 Comparison of predicted and measured spectral peak frequency and SPL for WICS bay

Model	Grid	K16 peak frequency, Hz	K16 peak SPL	K18 peak frequency, Hz	K18 peak SPL
SA–DES	Coarse	465 ± 15	165.4	465 ± 15	167.8
SA–DES	Medium	480 ± 15	162.3	480 ± 15	164.8
SA–DES	Fine	450 ± 15	159.5	465 ± 15	162.4
SST–DES	Coarse	465 ± 15	166.5	465 ± 15	169.6
SST–DES	Medium	480 ± 15	163.7	480 ± 15	167.4
SST–DES	Fine	465 ± 15	161.7	465 ± 15	164.1
SST–MS	Coarse	465 ± 15	164.8	465 ± 15	169.0
SST–MS	Medium	450 ± 15	163.0	450 ± 15	165.0
SST–MS	Fine	450 ± 15	164.6	450 ± 15	167.0
Data		459 ± 10	164.0	459 ± 10	164.9

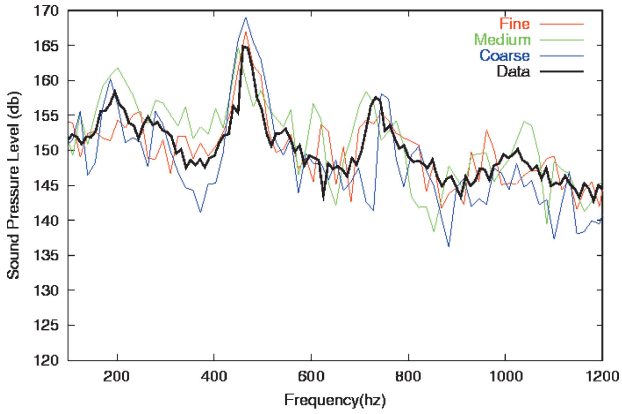

Fig. 31b SPL spectrum at K18 (back wall) location, SST–MS model.

Conclusions

The simulations performed indicate a fundamental difficulty in verification and validation for unsteady flows. As the grid is refined, smaller scale turbulent structures are resolved in the solution. This process will continue until the grid is refined below the Komologrov scale and all of the turbulent scales are grid resolved. The limiting grid-refinement case cannot be approached with current computing hardware for most real-world, high-Reynolds-number problems of interest. Comparison of statistical quantities derived from the unsteady solutions can be made to ensure that the important features of the unsteady flow have been captured with a given grid, but the nature of the statistical analysis makes it difficult to assess whether a true grid convergence has been achieved. The solutions performed in this study were shown to be statistically stationary using an overlapping window technique for a given grid-refinement level.

The time step study indicates that from 100 to 200 time steps per primary shedding cycle are required for temporal accuracy using a second-order time implicit algorithm with the SST–MS hybrid model for both of the test cases investigated in this study. Using a larger time step causes the primary spectral peak to occur at a lower frequency than is predicted with the smaller time step and lower than the frequency seen in the data.

The simulations for both test cases on the midlevel and fine-level grid systems using the SST-based hybrid models are in good general agreement, thus indicating that a level of grid convergence can be achieved for the large turbulent scales with these models. The SA–DES model did not reach grid convergence for the cylinder average drag in this refinement study, and this model produced the greatest variation in prediction of the spectral peak SPL for the weapons bay case. The sensitivity of the SA–DES model to grid density may indicate that a filter function that includes some measure of the local turbulence length scales is superior to a filter function that only includes the local grid scale. The turbulent length scale to grid length scale ratio was greater than two in the wake region of the cylinder and in the shear layer region of the bay for the midlevel and fine-level grid systems for both test cases. This may serve as a rule of

thumb for minimum grid resolution for hybrid model applications. The coarse-level grid is inadequate for all of the hybrid RANS/LES models tested on the cylinder case and tended to produce a RANS-like solution for all of the models tested. This indicates that all of the models will tend to the RANS limit if the grid spacing becomes too coarse to support the turbulent scales of the flow.

On the cylinder midlevel grid, the traditional RANS turbulence models tended to produce flows that display a single dominant shedding event, as can be seen by the larger and narrower spectral peak value of the normal-force PSD. All of the hybrid turbulence models produce solutions with a much broader spectral peak than the peak produced by the RANS models on the midlevel and fine-level grids. This indicates that the hybrid models are allowing weaker turbulent structures to exist at scales away from the primary shedding scale. These weaker structures are being suppressed in the RANS solutions.

All of the hybrid models transitioned from RANS to LES from the coarse grid to the mid grid on the circular cylinder. The grid spacings increase by a factor of two from the coarse grid to the medium grid. This indicates that the transition process from RANS to LES is quite sudden for all of the hybrid models tested. The nonphysical nature of the coarse-grid solution also points out that care must be taken to ensure the grid spacing is small enough to support the significant length scales of the unsteady flow or large errors may occur in the simulation.

The hybrid RANS/LES turbulence models are relatively new and will need to be exercised for a wide variety of problems to determine their accuracy before they become an accepted tool for fluid modelers. They seem to offer much for unsteady flow applications, but issues such as grid sensitivity need to be further addressed. All three of the models tested here produced results that are adequate for most engineering applications when applied to a suitably fine grid. The lack of experimental measurements for the detailed flow structure for both these test cases precludes drawing conclusions on the ability of these models to provide fine-grain details of the flow that may be required for some engineering applications. It is hoped that more effort will go into the validation of these models in the near future so that they can be matured for use in everyday applications.

Acknowledgment

This publication is made possible through support provided by the Department of Defense High Performance Computing Modernization Program Programming Environment and Training activities through Mississippi State University under terms of Contract N62306-01-D-7110.

References

[1]Nichols, R., and Tramel, R., "Applications of a Highly Efficient Numerical Method for Overset Mesh Moving Body Problems," AIAA Paper 97-2255, June 1997.

[2]Sinha, N., Dash, S., Chidambaram, N., and Findlay, D., "A Perspective on the Simulation of Cavity Aeroacoustics," AIAA Paper 98-0286, Jan. 1998.

[3]Spalart, P., Jou, W.-H., Strelets, M., and Allmaras, S., *Comments on the Feasibility of LES for Wings and on a Hybrid RANS/LES Approach*, edited by C. Liu and Z. Liu, Greyden Press, Columbus, OH, 1997.

[4]Travin, A., Shur, M., Strelets, M., and Spalart, P., "Detached-Eddy Simulations Past a Circular Cylinder," *Flow, Turbulence and Combustion*, Vol. 63, March 2000, pp. 293–313.

[5]Vatsa, V. N., and Singer, B. A., "Evaluation of a Second-Order Accurate Navier–Stokes Code for Detached Eddy Simulation past a Circular Cylinder," AIAA Paper 2003-4085, June 2003.

[6]Hansen, R. P., and Forsythe, J. R., "Large and Detached Eddy Simulations of Flow over a Circular Cylinder Using Unstructured Grids," AIAA Paper 2003-0775, Jan. 2003.

[7]Elmiligui, A., Abdol-Hamid, K., Massey, S., and Pao, S., "Numerical Study of Flow past a Circular Cylinder Using RANS, Hybrid RANS/LES and PANS Formulations," AIAA Paper 2004-4959, Aug. 2004.

[8]Baldwin, B. S., and Lomax, H., "Thin Layer Approximation and Algebraic Model for Separated Turbulent Flows," AIAA Paper 78-0257, Jan. 1978.

[9]Rizzetta, D. P., "Numerical Simulation of Supersonic Flow over a Three-Dimensional Cavity," *AIAA Journal*, Vol. 26, No. 7, 1988, pp. 799–807.

[10]Suhs, N. E., "Computations of Three-Dimensional Cavity Flow at Subsonic and Supersonic Mach Numbers," Arnold Engineering Development Center, Rept. AEDC-TR-88-30 (AD-B130517), Arnold AFB, TN, Feb. 1989.

[11]Baysal, O., Yen, G. W., and Fouladi, K., "Navier–Stokes Computations of Cavity Aeroacoustics with Suppression Devices," AIAA/Deutsche Gesellschaft für Luft- und Raumfahrt Paper 92-02-161, May 1992.

[12]Arunajatesan, S., Shipman, J. D., and Sinha, N., "Hybrid RANS–LES Simulation of Cavity Flow Fields with Control," AIAA Paper 2002-1130, Jan. 2002.

[13]Dix, R. E., and Bauer, R. C., "Experimental and Theoretical Study of Cavity Acoustics," Arnold Engineering Development Center, Rept. AEDC-TR-99-4 (AD-A384010), Arnold AFB, TN, May 2000.

[14]Nichols, R. H., and Nelson, C. C., "Application of Hybrid RANS/LES Turbulence Models," AIAA Paper 2003-0083, Jan. 2003.

[15]Rizzetta, D. P., and Visbal, M. R., "Large-Eddy Simulation of Supersonic Cavity Flowfields Including Flow Control," AIAA Paper 2002-2853, June 2002.

[16]Spalart, P. R., and Allmaras, S. R., "A One-Equation Turbulence Model for Aerodynamic Flows," AIAA Paper 92-0439, Jan. 1992.

[17]Constatinescu, G., and Squires, K., "LES and DES Investigations of the Turbulent Flow over a Sphere," AIAA Paper 2000-0540, Jan. 2000.

[18]Mitchell, A., Morton, S., and Forsythe, J., "Analysis of Delta Wing Vortical Substructures Using Detached-Eddy Simulation," AIAA Paper 2002-2968, June 2002.

[19]Forsythe, J., Squires, K., Wurtzler, K., and Spalart, P, "Detached-Eddy Simulation of Fighter Aircraft at High Alpha," AIAA Paper 2002-0591, Jan. 2002.

[20]Strelets, M., "Detached Eddy Simulation of Massively Separated Flows," AIAA Paper 2001-0879, Jan. 2001.

[21]Menter, F. R., and Rumsey, C. L., "Assessment of Two-Equation Turbulence Models for Transonic Flows," AIAA Paper 94-2343, June 1994.

[22]Nelson, C., and Nichols, R., "Evaluation of Hybrid RANS/LES Turbulence Models using an LES Code," AIAA Paper 2003-3552, June 2003.

[23]Tramel, R. W., and Nichols, R. H., "A Highly Efficient Numerical Method for Overset-Mesh Moving-Body Problems," AIAA Paper 97-2040, June 1997.

[24]Einfeldt, B., Munz, C. D., Roe, P. L., and Sjogreen, B., "On Godunov-Type Methods near Low Densities," *Journal of Computational Physics*, Vol. 92, No. 2, 1991, pp. 273–295.

[25]Nichols, R. H., and Heikkinen, B. D., "Validation of Implicit Algorithms for Unsteady Flows Including Moving and Deforming Grids," AIAA Paper 2005-0683, Jan. 2005.

[26]Nichols, R. H., and Nelson, C. C., "Wall Function Boundary Conditions Including Heat Transfer and Compressibility," *AIAA Journal*, Vol. 42, No. 6, 2004, pp. 1107–1114.

[27]Jones, G. W., Cincotta, J. J., and Walker, R. W., "Aerodynamic Forces on a Stationary and Oscillating Circular Cylinder at High Reynolds Number," NASA TR-R-300, Oct. 1968.

[28]Roshko, A., "Experiments on the Flow past a Circular Cylinder at Very High Reynolds Number," *Journal of Fluid Mechanics*, Vol. 10, Pt. 3, May 1961, pp. 345–356.

[29]Schlichting, H., *Boundary Layer Theory*, 7th ed., McGraw–Hill, New York, 1979, p. 32.

A. Karagozian
Associate Editor